



Article

Bifunctional Ag-Decorated CeO₂ Nanorods Catalysts for Promoted Photodegradation of Methyl Orange and Photocatalytic Hydrogen Evolution

Jinwen Liu ¹, Li Zhang ², Yifei Sun ³ and Yang Luo ^{1,*}¹ Third Institute of Oceanography, Ministry of Natural Resources, Xiamen 361005, China; jinwenliu@tio.org.cn² School of Environment and Civil Engineering, Dongguan University of Technology, Dongguan 823808, China; zzhangyige@163.com³ College of Energy, Xiamen University, Xiamen 361005, China; yfsun@xmu.edu.cn

* Correspondence: luoyang@tio.org.cn; Tel.: +86-0592-2195201; Fax: +86-0592-2086646

Abstract: The photodegradation of organic pollutants and photocatalytic hydrogen generation from water by semiconductor catalysts are regarded as the of the most promising strategies to resolve the crisis of global environmental issues. Herein, we successfully designed and prepared a series of silver-decorated CeO₂(Ag/CeO₂) photocatalysts with different morphologies by a facile hydrothermal route. The physical properties, charge transfer behavior and photocatalytic performances (degradation and hydrogen evolution) over diverse catalysts with nanocubes, nanoparticles and nanorods shapes were comprehensively studied. It was found that the Ag-decorated CeO₂ nanorods (Ag/R-CeO₂) demonstrate the best activity for both photocatalytic methyl orange (MO) degradation and photocatalytic H₂ production reaction with attractive stability during cycling tests, suggesting its desirable practical potential. The superior performance of Ag/R-CeO₂ can be ascribed to (1) the facilitated light absorption due to enriched surface oxygen vacancies (OVs) and plasmonic Ag nanoparticles on nanorods, (2) the facilitated photo-excited charge carrier (e⁻-h⁺) separation efficiency on a metal/oxide hybrid structure and (3) the promoted formation of active reaction intermediates on surface-enriched Ag and oxygen vacancies reactive sites on Ag/CeO₂ nanorods. This study provides a valuable discovery of the utilization of abundant solar energy for diverse catalytic processes.



Citation: Liu, J.; Zhang, L.; Sun, Y.; Luo, Y. Bifunctional Ag-Decorated CeO₂ Nanorods Catalysts for Promoted Photodegradation of Methyl Orange and Photocatalytic Hydrogen Evolution. *Nanomaterials* **2021**, *11*, 1104. <https://doi.org/10.3390/nano11051104>

Academic Editors:

Simelys Hernández and José Luis Cagide Fajín

Received: 13 April 2021

Accepted: 23 April 2021

Published: 24 April 2021

Publisher's Note: MDPI stays neutral with regard to jurisdictional claims in published maps and institutional affiliations.



Copyright: © 2021 by the authors. Licensee MDPI, Basel, Switzerland. This article is an open access article distributed under the terms and conditions of the Creative Commons Attribution (CC BY) license (<https://creativecommons.org/licenses/by/4.0/>).

Keywords: photocatalytic degradation; photocatalytic hydrogen evolution; catalyst; Ag/CeO₂; oxygen vacancy

1. Introduction

The rapid development of industry leads to the large consumption of fossil fuels, which has brought inevitable environmental issues. Specifically, the massive emission of CO₂ and water pollution of organic compounds severely threaten ecosystems and human health [1–3]. Therefore, the purification of dye-polluted wastewater and the exploration of clean energy carriers such as H₂ are two huge challenges for humans to pursue sustainable development [4,5].

As the most representative dye, methyl orange (MO) is not decomposable at ambient conditions [6]. Until now, enormous efforts have been undertaken to develop diverse technologies for the efficient degradation of MO [7]. The pioneering work of the photoreduction of organic pollutant using TiO₂ photocatalyst can date back to 1979 [8], from which photocatalytic degradation has received extensive studies [9,10]. For decades, the photodegradation of MO using semiconductor photocatalysts has been paid immense attention due to the abundance of solar energy, low cost and easy operability of the reaction system [11]. Additionally, diverse kinds of photocatalysts have been reported to be active for photocatalytic degradation. For example, transition metal oxides including

ZnO [12], TiO₂ [13] and Co₃O₄ [14] with the optical bandgap smaller than the wavelength of UV irradiation, fast charge transfer efficiency, and suitable VB/CB positions for corresponding oxidation/reduction reactions were reported as efficient photocatalysts. The photogenerated electron (e⁻) and hole (h⁺) can combine with O₂ and OH⁻ dissolved in water to formulate ·O₂⁻ and ·OH, respectively [6], and all these oxygen-containing species are highly active for the decomposition of organic pollution molecules. Different from MO degradation, mainly using photo-excited h⁺, the photocatalytic water splitting takes advantage of the photo-excited e⁻ to reduce proton in water and generate H₂ [15]. It is widely accepted that the quantity and prolonged lifetime of these active photo-generated e⁻ and h⁺ is tightly linked to the enhanced photocatalytic performance [16,17].

CeO₂, with a low price, robustness, nontoxicity and high redox capability, has obtained tremendous attention in the field of optics [18], electrochemistry [19] and thermocatalysis [2,20]. The surface of CeO₂ crystal is rich with oxygen vacancies (OVs) due to the emergence of the Ce³⁺/Ce⁴⁺ redox pair, which enables the efficient manipulation of band structure and light absorption [21,22]. Recent research has illustrated that the surface OVs of CeO₂ nanocrystals can be tuned by controlling its exposure facets and morphology [23,24]. The crystal facet with weak Ce-O bond strength is favorable for the formation of OVs. This discovery offers a brand-new way to manipulate the optical property of CeO₂ and further the potential photocatalytic performance.

Besides the manipulation of intrinsic property, some precious metal nanoparticles, for instance Pt and Au, were post-deposited onto CeO₂ as the co-catalyst to accelerate the separation of photo-excited e⁻-h⁺ pairs and delay recombination through h⁺ trapping by the extra generation of extra hydroxyl species [25,26]. For example, Au@CeO₂ nanocomposite exhibited higher activity and stability in the photocatalytic degradation of methyl orange and methylene blue, while compared to pristine CeO₂ [27]. Pt/CeO_x/TiO₂ was attested to be a promising catalyst for the photocatalysis in water splitting, and the H₂ productivity was approximately seven times higher than the benchmark of WO₃ [28]. However, the noble metals, with a high price and scarcity strongly restricted its large-scale utilization [16]. Thereby, the design of an efficient photocatalyst functionalized by a non-noble metal cocatalyst is highly desirable.

It is reported that Ag nanoparticles hold a big promise in wastewater disposal applications due to their controllable biocompatibility and excellent antibacterial activity [29]. Additionally, Ag can serve as the co-catalyst, substituting expensive Au or Pt, to modify the surface properties of semiconductor photocatalysts. For example, Ag-modified ZnO was proved to be an effective catalyst for the photocatalytic organic pollutant degradation. The conversion of Ag to Ag⁺ by a dissolved oxygen molecule resulted in the formation of large amount of active oxygen groups (HO₂· and ·OH), benefitting the degradation efficiency [30]. However, the traditional post-deposition method such as impregnation or post-photo-deposition usually added complexity to the fabrication process, which also led to the uneven distribution of Ag particles and poor metal-oxide adhesion [31]. A new design principle to prepare Ag-decorated CeO₂ with enriched surface OVs is urgently required, which is expected to promote photocatalytic performance for both MO degradation and H₂ production.

Following this line of thinking, in this paper, we develop a readily available and convenient one-step solvothermal approach to fabricate a series of Ag-modified CeO₂ photocatalysts with the morphologies of nanocubes, nanoparticles and nanorods, respectively. By applying a set of characterizations and measurements, it was discovered that the Ag-decorated CeO₂ nanorods possess superior performance and stability for not only photocatalytic degradation, but also hydrogen evolution. The underlying mechanism of improved performance was presented based on the systematic characterization results, which is suggestive and constructive for the future design of novel semiconductor photocatalysts.

2. Materials and Methods

2.1. Materials

The chemicals utilized in this work were analytical reagent grade and underwent no further purification. Deionized (DI) water was used throughout the study. $\text{Ce}(\text{NO}_3)_3 \cdot 6\text{H}_2\text{O}$, $\text{Ag}(\text{NO}_3)_2$, NaOH , NaBH_4 and ethanol were received from Sinopharm Chemical Reagent Co., Ltd, Shanghai, China.

2.2. Photocatalysts Preparation

Synthesis of CeO_2 catalyst CeO_2 were fabricated via a hydrothermal method [25]. To obtain CeO_2 , $\text{Ce}(\text{NO}_3)_3 \cdot 6\text{H}_2\text{O}$ (3.48 g) was dissolved in 5 mL of DI water (A) and NaOH was dissolved in 35 mL of DI water (B). Then, the solutions A and B were mixed well with magnetic stirring. After 30 min, the as-obtained white solution (A + B) was poured into a Teflon lined stainless steel autoclave with 100 mL volume without stirring, and the hydrothermal treatment was performed for 24 h. Afterwards, the autoclave was cooled to room temperature naturally. The obtained white production was gathered by centrifuging and was alternately washed thoroughly via ethanol and deionized water for several times until the $\text{pH} = 7$. Finally, the composites were kept in an oven at 80°C for 12 h to get CeO_2 . The amount of NaOH and hydrothermal treatment temperature were changed for different shapes of CeO_2 (nanorod: $\text{NaOH} = 9.8$ g, temp = 100°C , nanocube: $\text{NaOH} = 9.8$ g, temp = 180°C , nanoparticle: $\text{NaOH} = 0.014$ g, temp = 100°C). The CeO_2 shapes of nanorods, nanocubes and nanoparticles were marked as R- CeO_2 , C- CeO_2 and P- CeO_2 , respectively.

Synthesis of Ag/ CeO_2 catalyst Ag/ CeO_2 were also fabricated via a hydrothermal method. Similar to the method shown above, after we obtained the solution of A + B, 0.082 g of AgNO_3 was mixed into the solution. After stirring for another 20 min, NaBH_4 (0.2 g) was finally put into the mixture. Then, the above solution was hydrothermally treated at 180°C for 24 h in a Teflon lined stainless steel autoclave (100 mL). The obtained production was gathered by centrifuging and was alternately washed via ethanol and deionized water until the $\text{pH} = 7$. Finally, the composites were put down in an 80°C oven and kept there for 12 h to obtain Ag/C- CeO_2 . The synthesis Ag/ CeO_2 nanorods was similar to Ag/C- CeO_2 except that the temperature was changed from 180°C to 100°C . The composite was denoted as Ag/R- CeO_2 , while the synthesis process of Ag/ CeO_2 nanoparticles was similar to Ag/R- CeO_2 except that the amount of NaOH was changed from 9.8 g to 0.014 g for Ag/P- CeO_2 . The sample was denoted as Ag/P- CeO_2 .

The abbreviations of all samples are listed in Table 1.

Table 1. Samples.

Photocatalyst	Abbreviation
CeO_2 nanocubes	C- CeO_2
CeO_2 nanoparticles	P- CeO_2
CeO_2 nanorods	R- CeO_2
Ag decorated C- CeO_2	Ag/C- CeO_2
Ag decorated P- CeO_2	Ag/P- CeO_2
Ag decorated R- CeO_2	Ag/R- CeO_2

2.3. Sample Characterization

The X-ray diffraction (XRD) patterns were recorded using an X-ray powder diffractometer (Panalytical X'pert Pro Super, Malvern, UK) along with radiation of $\text{Cu K}\alpha$. For each sample, 20° to 80° of 2θ (Bragg's angles) were conducted under a $10^\circ/\text{min}$ rate. Transmission electron microscopy (TEM) images were received via a TECNAI F-20 apparatus. SEM (Scanning electron microscopy) images were observed using ZEISS-SIGMA. A UV-vis Cary5000 spectrometer (VARIAN Company, Palo Alto, CA, USA) using BaSO_4 reference was used to obtain UV-visible diffuse reflection spectra (UV-vis DRS). An instrument of F-7000 spectrophotometer was conducted to gain photoluminescence (PL) spectra and the

excitation wavelength was 325 nm. Photocurrents (PCs) of the resultant catalysts were observed with a CHI660E electrochemical analyzer, attaching a home-made standard three-electrode quartz cell. Sample suspensions dropped directly and coated onto the precleaned ITO (indium tin oxide) glass surface were used as work electrodes. An SCE (saturated calomel electrode) electrode acted as the reference and the Pt wire served as a counter electrode. Na₂SO₄ aqueous solution (0.2 M) without other additives served as the electrolyte. The irradiation light was an Hg lamp (500 W, the accumulated intensity: 110 mW/cm²). The work electrode (0.95 cm²) was exposed to the Na₂SO₄ electrolyte. A bias potential of 0.1 V (vs. Ag/AgCl) was applied. UV–Vis Raman System Invia manufactured by Renisha using a laser Raman spectrometer was performed to observe the Raman test. The excitation source was a 532 nm laser, and the scanning wave number range is specified in this paper.

2.4. Catalytic Activity Assessment

The photocatalytic degradation performance of pristine CeO₂ and Ag/CeO₂ composites were evaluated by degrading MO under a 500 W Hg lamp (NBT Science Co. Ltd. China, $\lambda = 200\text{--}1100$ nm, the accumulated intensity: 110 mW/cm²) illumination, positioned at a distance of 5 cm over the photocatalytic reactor. Experiments were conducted at ambient temperature. Typically, 50 mg of the resultant photocatalyst was decentralized in a 100 mL MO pollutant solution (5 mg/L, pH = 6.5–7.0). In order to achieve the adsorption and desorption equilibrium of the photocatalyst, MO and water, the above mixture was kept at magnetic stirring (the speed of magnetic stirrer is 300 r/min) for 20 min in the chamber under dark ahead of light irradiation. With magnetic stirring, the suspension was exposed to light irradiation. The collection of 4 mL of solution from the reaction suspension every 20 min was centrifuged to eliminate the photocatalyst. Then, the concentrations of MO dye in every sample were analyzed via a UV–vis spectrophotometer at 464 nm (MO characteristic absorbance).

Photocatalytic H₂ evolution reaction tests of the samples were conducted using a reaction cell reactor with the volume of 500 mL. An amount of 0.10 g powder catalyst was decentralized in a mixture solution containing 180 mL of H₂O, H₂PtCl₆ solution and 20 mL of methanol (as a sacrificial reagent). H₂PtCl₆ solution was photo-reduced to obtain Pt (0.5 wt%) cocatalyst modified catalyst in the water splitting experiments. Then, the reactor was degassed via a pump. To establish the balance between adsorption and desorption, the mixture was kept for 20 min (300 r/min) under magnetic stirring prior to irradiation. The light source was a 300 W Xe lamp (Beijing China Education Au—Light Co., Ltd., Beijing, China, the accumulated intensity: 450 mW/cm²), positioned at a distance of 5 cm over the photocatalytic reactor. For the sake of maintaining the experiment temperature, a water cooling system was used around the photoreactor. A thermal conductivity detector from GC 2060 gas chromatograph served to monitor the amount of H₂. Additionally, the carrier gas was high-purity N₂.

3. Results and Discussion

First, XRD characterization was employed to explore the crystal structure of various catalysts, and the results are shown in Figure 1. The diffraction peaks at 28.5, 33.1, 47.5, 56.3, 59.1, 69.4, 76.7, and 79.1 degrees emerged on all CeO₂ samples can be assigned to (111), (200), (220), (311), (222), (400), (331), and (420) CeO₂ planes, respectively, suggesting the pure cubic fluorite structure (JCPDS 81-792) of all the CeO₂ [32,33]. Interestingly, the sharper diffraction peak could be seen on CeO₂ cubes, which could be ascribed to its larger crystal size [25]. In comparison, much weakened and broader diffraction peak are observed on R-CeO₂, suggesting the low crystallinity and partially disordered modality of CeO₂ with a nanorod shape.

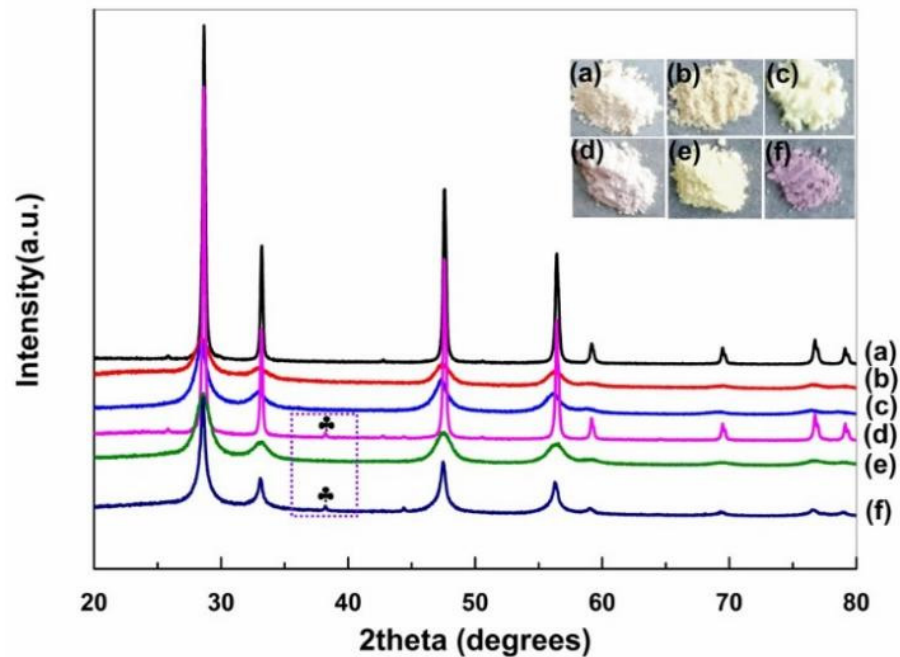


Figure 1. Photographs and XRD patterns of C-CeO₂ (a), (b) P-CeO₂, R-CeO₂ (c), (d) Ag/C-CeO₂, Ag/P-CeO₂ (e), and (f) Ag/R-CeO₂.

After introducing Ag, the diffraction peak of Ag (111) at 38.6° (the purple rectangle area in Figure 1) emerged on Ag/R-CeO₂ and Ag/C-CeO₂, evidencing the successful decoration of Ag. From the perspective of apparent optical property, the CeO₂ nanocubes showed a gray–white color, while the nanoparticles and nanorods samples were yellow and bright yellow, respectively. Nevertheless, after introducing Ag, those samples' colors significantly changed, indicating the alternation of optical property. Specifically, Ag/C-CeO₂ became light purple and Ag/R-CeO₂ turned to dark purple (inset of Figure 1a).

SEM was then utilized to characterize the detailed morphology of as-prepared CeO₂ and Ag/CeO₂ nanocomposites. As can be seen in Figure 2a, the C-CeO₂ displayed a quasi-cubic shape with a side length of approximately 20–100 nm. Meanwhile, the diameter of the round-shape CeO₂ particles was ~50 nm and the length of the CeO₂ nanorods was between 20–100 nm. The SEM images in Figure 2d–f shows that the CeO₂ with different shapes maintained their original morphology after the introduction of Ag nanoparticles. Moreover, the detailed morphology and lattice structure of Ag/R-CeO₂ were characterized by TEM, TEM-EDX and high-resolution TEM (HR-TEM). The Ag/R-CeO₂ with the rod-shape obtained the uniform diameter of around 20 nm (Figure 3a). The HR-TEM images (Figure 3b) demonstrated a lattice spacing of 0.19 nm, which is assignable to the (110) plane of fluorite structure CeO₂ [34], while the Ag nanoparticles with a small diameter of around 3 nm could also be detected. The interplanar distance of 0.24 nm is consistent with the Ag (111) plane [35]. Moreover, the interface between CeO₂ and Ag could be observed clearly. The TEM-EDX images shown in Figure 3c demonstrate the even distribution of all elements, including O, Ce and Ag, which are in line with the above XRD analysis that the Ag nanoparticle is successfully decorated onto the CeO₂ nanorod.

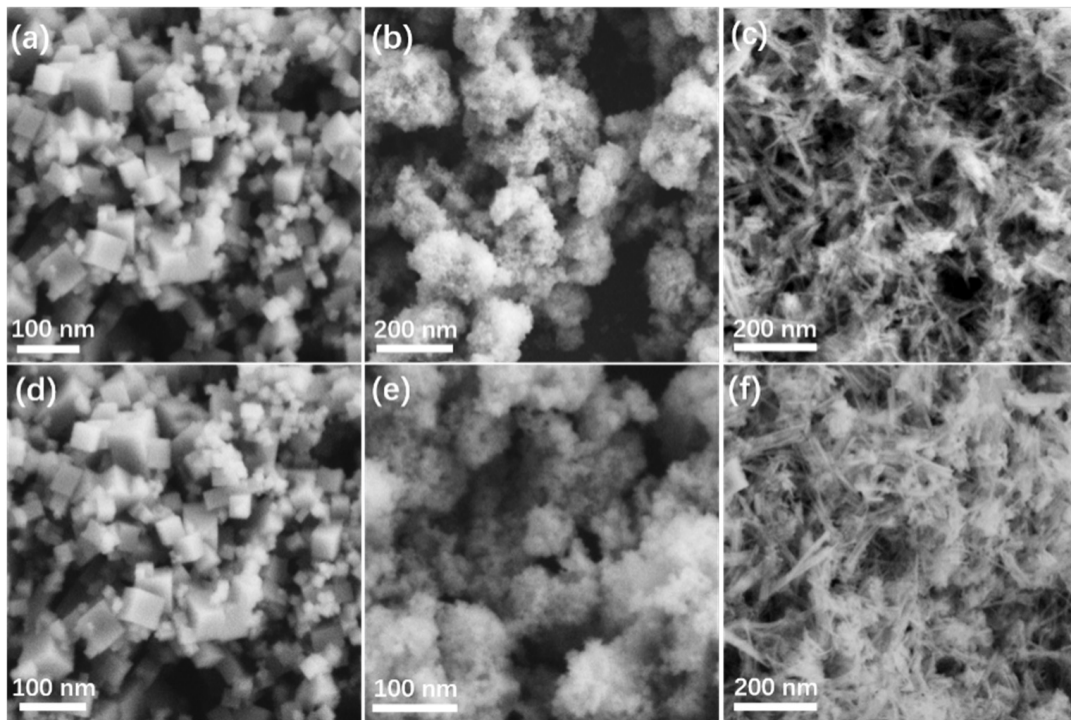


Figure 2. SEM images of various samples (a–f) corresponding to C-CeO₂, P-CeO₂, R-CeO₂, Ag/C-CeO₂, Ag/P-CeO₂, and Ag/R-CeO₂, respectively.

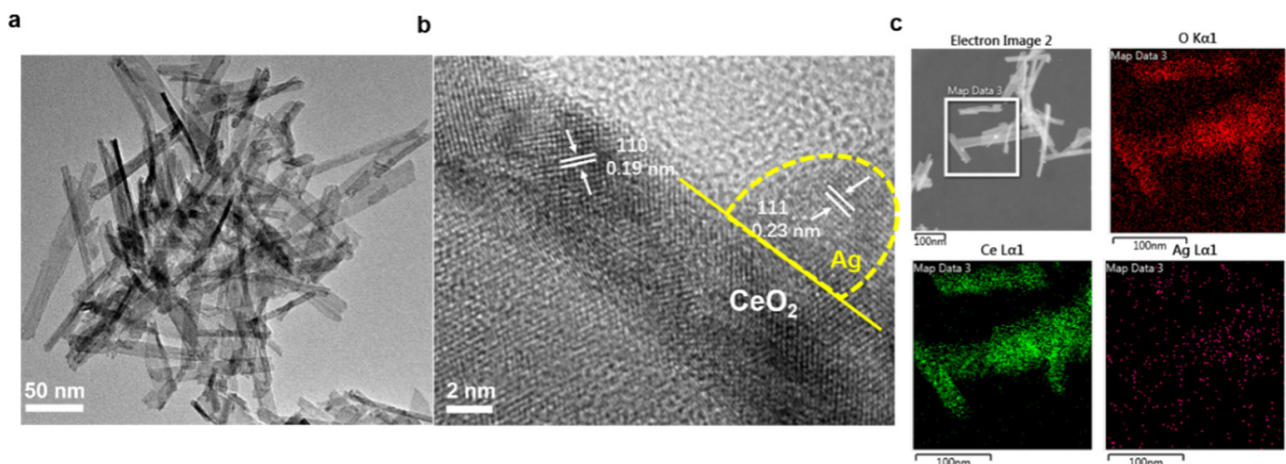


Figure 3. TEM (a), HRTEM (b) and TEM-EDX (c) images of sample Ag/R-CeO₂.

The UV–Vis DRS spectra of C-CeO₂, Ag/C-CeO₂, P-CeO₂, Ag/P-CeO₂, R-CeO₂ and Ag/R-CeO₂ samples are shown in Figure 4a, which confirms the optical absorption property of the samples with different morphologies. The absorption spectrum of R-CeO₂ significantly shifts to a higher wavelength, as compared to those of P-CeO₂ and C-CeO₂, suggesting that the R-CeO₂ exhibits a much stronger absorbance in the low frequency region. The Tauc equation was applied to determine the bandgap energy (E_g) of different CeO₂ [36]:

$$(\alpha h\nu)^n = A(h\nu - E_g)$$

where α , n , A and E_g correspond to the absorption coefficient, the light frequency, a constant and optical band gap, respectively. The n of CeO₂ is equal to 2 [37]. The E_g of the CeO₂ samples can be computed from the $(\alpha h\nu)^n$ versus $(h\nu)$ plot depiction (shown in Figure 4c). The bandgap values are reported in Table 2. The R-CeO₂ owns the smallest bandgap energy of 3.04 eV, which is much smaller than that of C-CeO₂ and P-CeO₂. Before, it was reported

that the E_g of CeO_2 could be manipulated by changing the morphologies and sizes of the crystal [38], and the light absorption ability is closely related to the optical bandgap of the material. Hence, it is reasonable to speculate that R- CeO_2 , with the smallest bandgap, should obtain the highest light absorption capability.

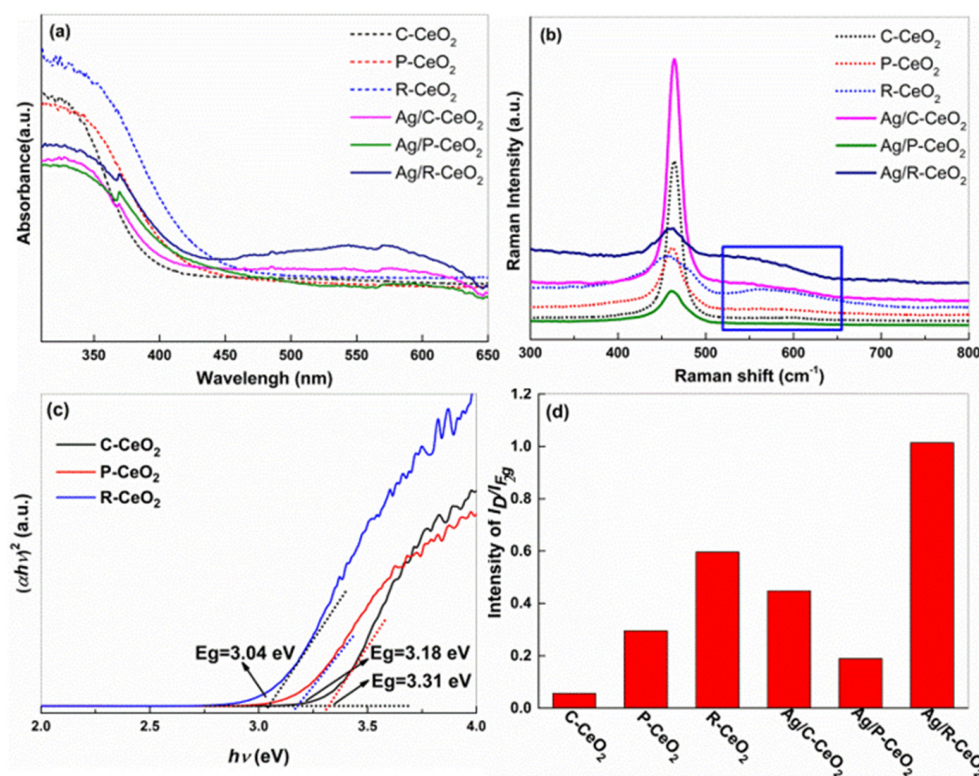


Figure 4. (a) UV-vis DRS, (b) Raman spectra, (c) plot of $(\alpha h\nu)^2$ versus $h\nu$ and (d) the intensity of I_D/I_{F2g} in Raman spectra of different CeO_2 and Ag/ CeO_2 .

Table 2. Bandgap values.

Photocatalyst	Bandgap Energy (eV)
C- CeO_2	3.31
P- CeO_2	3.18
R- CeO_2	3.04

After the decoration of Ag, the greatly boosted visible light (vis-light) absorption (~ 600 nm) could be observed on Ag-R- CeO_2 samples. The phenomenon could be explained by the surface plasmon resonance (SPR) effect of Ag, which was also found on other reported Ag modified catalysts [39,40]. On the surface decorated with SPR excitation of Ag metal, light can be captured and confined nearby Ag, and the Ag nanoparticles' resonance can play the role in improving the absorption of light for semiconductors [35,39,41], and further enhancing the photocatalytic activity.

Raman spectroscopy with a 532 nm excitation laser was further employed to disclose the vibration information of metal–oxygen bond, as demonstrated in Figure 4b. The Raman spectra of all CeO_2 possess the characteristic peaks at 462 cm^{-1} which can be imputed to the F_{2g} symmetric stretching vibrations pattern of fluorite CeO_2 structure [41]. The peak at $530\text{--}600\text{ cm}^{-1}$ could be assigned to the band of defect-induced (D), which is directly linked to the presence of defects or OVs in CeO_2 [42]. The relative intensity ratio of I_D/I_{F2g} can be applied to determine the relative concentration of OVs in different samples. Apparently, this ratio for R- CeO_2 ($I_D/I_{F2g} = 0.596$) is much higher than those of C- CeO_2 ($I_D/I_{F2g} = 0.056$) and P- CeO_2 ($I_D/I_{F2g} = 0.295$) samples, suggesting that R- CeO_2 possesses

the largest amount of OV_s (Figure 4d). After the loading of Ag, the relative intensity ratio of I_D/I_{F2g} Ag/R-CeO₂ sample drastically increases to 1.014, which is around two times larger than that of pure R-CeO₂, indicating the surging content of OV_s. This is partially due to the additive of the highly reducible agent of NaBH₄ during fabrication. Additionally, this phenomenon was in line with the results reported in the previous literature [34,43,44] that the loaded noble metal (such as Ru, Ag, Pt) could facilitate the generation of OV_s [34,35,45]. The surface decoration of Ag nanoparticles is able to activate the surface lattice oxygen to create more OV_s [34].

The photocatalytic property of the CeO₂ and Ag/CeO₂ with various morphologies were utilized for the photocatalytic MO dye degradation, and the results are shown in Figure 5a. The blank trial of the decolorization of MO dye verifies that only 15% and 12% of MO can be naturally degraded without catalysts (irradiation only) or without light irradiation (with Ag/R-CeO₂ only), respectively. This result could be explained by the self-photosensitized reaction of MO dye and absorption process of Ag/R-CeO₂ [31,46,47]. When both light irradiation and catalysts were applied, the degradation efficiency of MO was remarkably promoted, implying the synergistic effect between catalyst and light excitation. All the CeO₂ nanocomposites exhibit moderate photocatalytic activity, and the R-CeO₂ decreased the concentration of MO by ~60% after 160 min treatment. This performance was much better than that of CeO₂ nanoparticles (~20%) and CeO₂ nanocubes (~50%). After the introduction of Ag, the degradation rate of MO dye was further improved on all samples. More than 80% of MO was decomposed for the sample Ag/R-CeO₂ after light irradiation for 160 min, whereas about 41% of MO can be degraded over Ag/C-CeO₂ and 59% of MO be degraded over Ag/P-CeO₂. The kinetic linear modeling results of CeO₂ and Ag/CeO₂ are shown in Figure 5b; the degradation process followed a first order kinetic [48], and the Ag/R-CeO₂ displays the largest kinetic constant of 0.00969 min⁻¹, suggesting its highest conversion rate. To further confirm the degradation performance on Ag/R-CeO₂, the time-dependent UV-vis absorption spectra of MO concentration on Ag/R-CeO₂ are shown in Figure 5c. The wavelength of about 420 nm is confirmed for the absorbance of MO. Obviously, the intensity of MO absorbance declined rapidly as the treatment time increased, indicating the consumption of MO. Additionally, based on the result of UV-vis absorbance spectra, no other absorbance band could be detected, revealing that the conjugated structure of MO is destroyed molecules and no other intermediate product is formed [46,49,50].

The stability of the photocatalytic property for the MO degradation over Ag/R-CeO₂ was further investigated via cycling experiments. Five continuous tests were conducted without renewing the photocatalyst. The procedure of each independent measurement was identical except for refilling the MO solution for each run. After each measurement, the Ag/R-CeO₂ catalyst was re-collected by centrifugation, rinsed and dried for next cycle. It can be seen from Figure 6 that only a slight drop of degradation performance of MO is observed after five cycles, suggesting the desirable stability of the catalyst. This may be due to the loss of the catalyst during each round of catalyst collection, which is universal in the previous literature [51].

The measurement of the photocatalytic activity of hydrogen evolution on different CeO₂ and Ag/CeO₂ catalysts were also performed, and the results are given in Figure 7. R-CeO₂ shows the highest performance under the simulated solar irradiation. The average hydrogen evolution rates are 157, 109 and 56 μmol h⁻¹ g⁻¹ for R-CeO₂, P-CeO₂ and C-CeO₂, respectively (shown in Figure 7b). This order is consistent with that of the OV content on different samples. In addition, after the introduction of Ag, the hydrogen evolution rate was significantly improved, and the rate of H₂ production for Ag/R-CeO₂ rose from 157 to 316 μmol h⁻¹ g⁻¹ for Ag/R-CeO₂. These results indicate that besides OV_s, the Ag also exhibits another prominent influence on such an enhancement of performance.

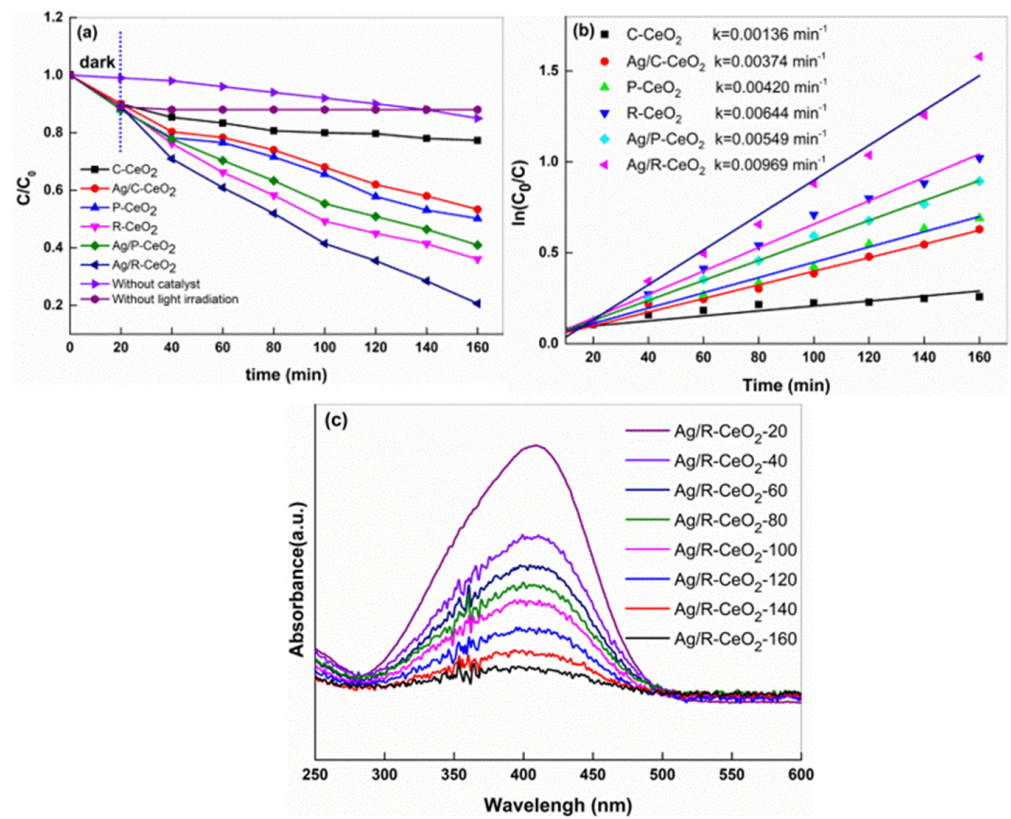


Figure 5. (a) The activities over different shapes of CeO₂ and Ag/CeO₂ on MO dye, (b) kinetic linear modeling and (c) UV–visible spectral changes of MO in aqueous at different irradiation intervals for Ag/R-CeO₂ under light illumination.

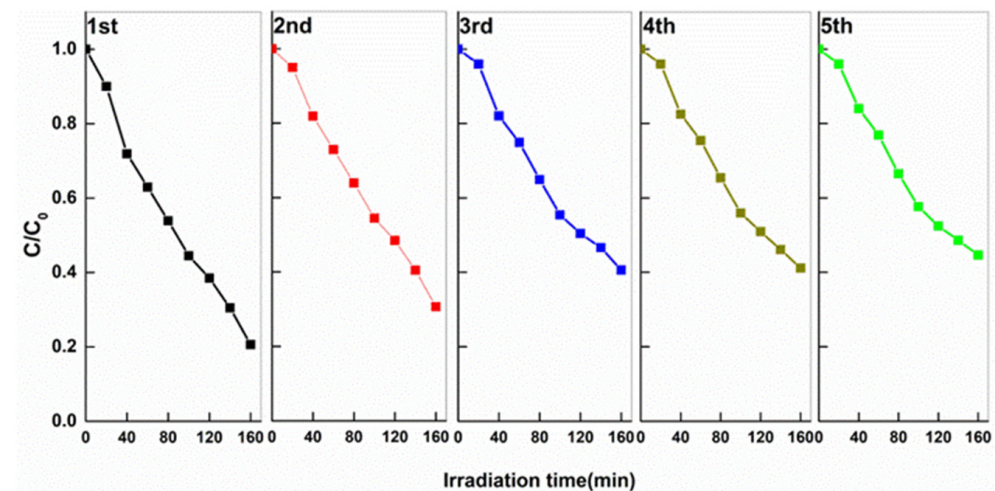


Figure 6. Successive test run for the degradation of MO in aqueous on Ag/R-CeO₂.

Usually, photo-excited charge separation efficiency is the key effect in determining the photocatalytic degradation performance and hydrogen evolution of a semiconductor photocatalyst. Therefore, to figure out the mechanism of promoted activity on Ag/R-CeO₂, the separation efficiency of photo-induced charge carriers was performed by the PL analysis at room temperature with an excitation wavelength of 325 nm. The PL spectra for all as-prepared samples are displayed in Figure 8a. Obviously, a shoulder emission peak of around 400 nm can be detected with the excitation wavelength at 325 nm, which stems from the intrinsic luminescence of CeO₂. The emission intensity of Ag/CeO₂ is much inferior to that of CeO₂, suggesting that the recombination of carriers is suppressed

after the loading of Ag. Our experimental observations are in agreement with a previous report that the deposition of Ag metal nanoparticles can accelerate the separation and transportation of photogenerated carriers, further resulting in the quenching effect of PL intensity [19,52]. Additionally, compared to Ag/P-CeO₂ and Ag/C-CeO₂, the sample Ag/R-CeO₂ has lowest emission intensity, meaning that the OVVs can also help prevent the recombination of photo-excited charge carrier. The transient photocurrent (PC) of the samples was also exploited to investigate the excitation and transfer of photo-induced e⁻ and h⁺. As shown in Figure 8b, upon irradiation, a quick photocurrent response was clearly given on all the samples and the transient PC density of Ag/CeO₂ is much higher than the other two CeO₂ during the continuous several light on-off cycles. In addition, Ag/R-CeO₂ possesses the highest PC density in all Ag/CeO₂ samples, meaning the larger amount of photoinduced electrons on the surface could be rapidly transferred.

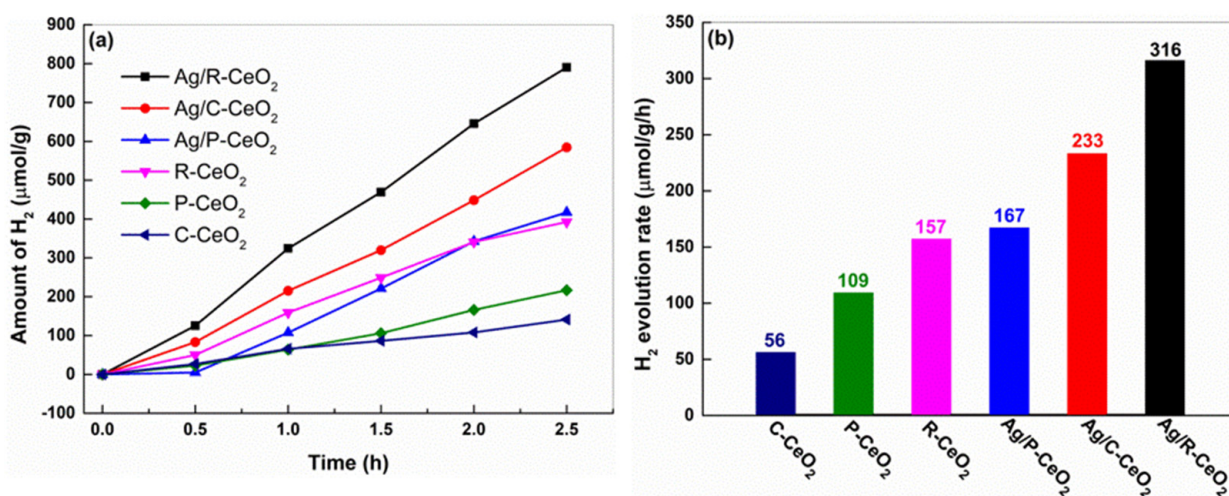


Figure 7. (a) The time dependent photocatalytic hydrogen evolution performance plot. (b) summary of photocatalytic H₂ evolution rates over the different resultant samples.

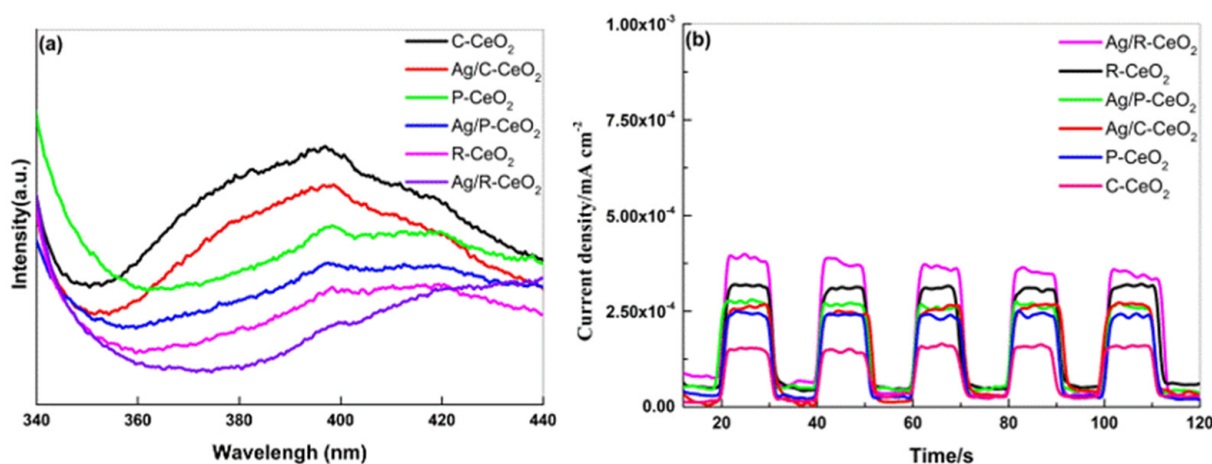


Figure 8. PL emission spectra (a) and the photocurrent responses (b) of all as-prepared samples.

Based on the analysis above, the enhanced photocatalytic degradation/hydrogen evolution performance of the Ag/R-CeO₂ nanorods' photocatalyst can be understood and explained by the possible mechanism proposed in Figure 9. Upon the photocatalyst being irradiated by the Hg lamp, CeO₂ was activated to produce the e⁻ and h⁺. First of all, the Ag/R-CeO₂ with rich OVVs and plasmonic Ag nanoparticles narrowed the optical bandgap and benefits the light absorption. Secondly, both OVVs and Ag facilitated the generation of a larger amount of photo-excited charge carrier and suppressed their recombination

simultaneously. Then, these alive e^- and h^+ with prolonged lifetime combined with water-dissolved O_2 and OH^- to create highly oxidative $\cdot O_2^-$ and $\cdot OH$ to accelerate the decomposition of MO.

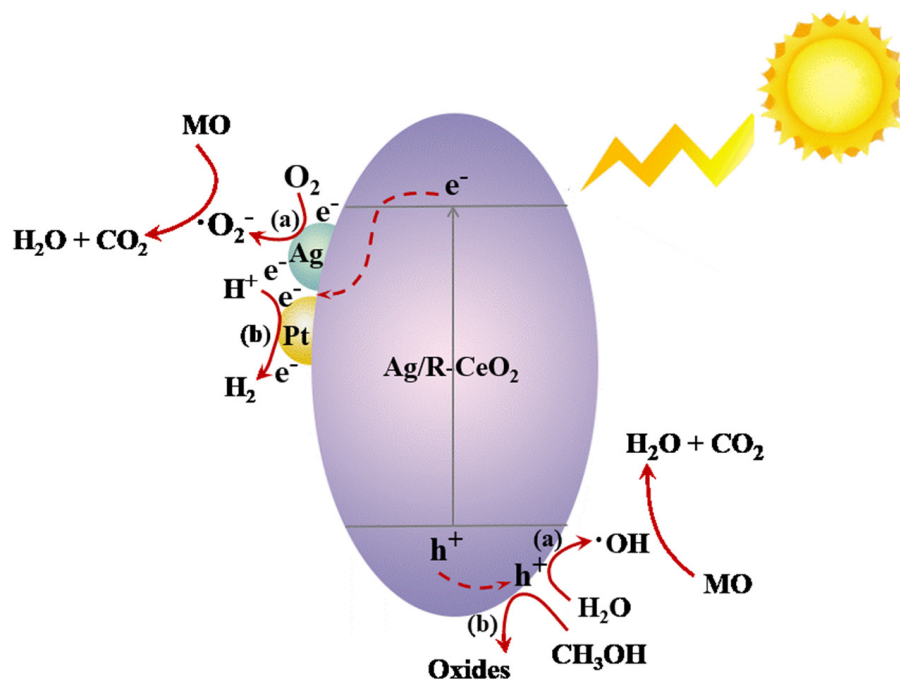


Figure 9. Schematic of the photocatalytic degradation action of MO and photocatalytic water splitting on the Ag/R-CeO₂ photocatalyst.

In addition, the surface OVs may play another important role in the absorption of dissolved oxygen molecule, which can furnish more effective surface reaction sites for photocatalytic degradation, while for the photocatalytic water splitting process, the accumulated photoelectrons quickly transferred to surface Ag and Pt nanoparticles to react with protons for hydrogen production. Therefore, the photocatalytic hydrogen evolution performance can be significantly enhanced.

4. Conclusions

In this work, we successfully synthesized a series of Ag/CeO₂ nanocubes, nanoparticles and nanorods' photocatalysts via a facile one-step hydrothermal process. The photocatalytic degradation of MO and photocatalytic hydrogen evolution reaction of the catalysts demonstrate strong morphology dependence and the Ag/CeO₂ nanorods possess the highest photocatalytic activity for both reactions due to the following reasons: (1) the catalyst with a different shape shows a distinctive surface OV concentration and the CeO₂ nanorods demonstrate the largest amount of OV concentration. The OVs and surface decoration of Ag with the SPR effect collectively leads to the narrowing of the optical band gap, the increase in light absorption, the prolonged lifetime of the charge carrier and the improvement of photocatalysis performance. (2) The decoration of Ag nanoparticles on CeO₂ nanorods can also prevent the recombination of e^- - h^+ pairs by efficient electron transfer from CeO₂ to Ag, leading to the charge separation efficiency and enhanced photocatalytic hydrogen evolution performance. (3) Moreover, both Ag and OVs can serve as a reactive site to facilitate the adsorption of O_2 and OH^- to form highly active $\cdot O_2^-$ and $\cdot OH$ for photocatalytic degradation. This study is believed to shed light on the exploration of well-designed photocatalysts toward diverse photocatalytic processes.

Author Contributions: J.L. offered the idea and wrote the manuscript; L.Z. performed the experiments, Y.S. and Y.L. discussed the experiments and participated in writing manuscript. All authors have read and agreed to the published version of the manuscript.

Funding: This work is financially supported by National Key R&D Program of China, grant number 2019YFD0901105, National Science Foundation of Fujian Province, China, grant number 2018J01062.

Data Availability Statement: Not applicable.

Acknowledgments: The author gratefully acknowledges the funding received from Jianhui Li Research Group, the College of Energy, Xiamen University, Xiamen 361005, China.

Conflicts of Interest: The authors declare no conflict of interest. The funders had no role in the design of the study; in the collection, analyses, or interpretation of data; in the writing of the manuscript, or in the decision to publish the results.

References

1. Ajmal, A.; Majeed, I.; Malik, R.; Idriss, H.; Nadeem, A. Principles and mechanisms of photocatalytic dye degradation on TiO₂ based photocatalysts: A comparative overview. *RSC Adv.* **2014**, *4*, 37003–37026. [[CrossRef](#)]
2. Gu, S.; Chen, Y.; Yuan, X.; Wang, H.; Chen, X.; Liu, Y.; Jiang, Q.; Wu, Z.; Zeng, G. Facile synthesis of CeO₂ nanoparticle sensitized CdS nanorod photocatalyst with improved visible-light photocatalytic degradation of rhodamine B. *RSC Adv.* **2015**, *5*, 79556–79564. [[CrossRef](#)]
3. Zheng, Y.; Liu, Y.; Guo, X.; Chen, Z.; Zhang, W.; Wang, Y.; Wang, Y.; Tang, X.; Zhang, Y.; Zhao, Y. Sulfur-doped g-C₃N₄/rGO porous nanosheets for highly efficient photocatalytic degradation of refractory contaminants. *J. Mater. Sci. Technol.* **2020**, *41*, 117–126. [[CrossRef](#)]
4. Wang, J.; Wang, G.; Cheng, B.; Yu, J.; Fan, J. Sulfur-doped g-C₃N₄/TiO₂ S-scheme heterojunction photocatalyst for Congo Red photodegradation. *Chin. J. Catal.* **2021**, *42*, 56–68. [[CrossRef](#)]
5. Feng, L.; Zou, Y.; Li, C.; Gao, S.; Zhou, L.-J.; Sun, Q.; Fan, M.; Wang, H.; Wang, D.; Li, G.; et al. Nanoporous sulfur-doped graphitic carbon nitride microrods: A durable catalyst for visible-light-driven H₂ evolution. *Int. J. Hydrogen Energy* **2014**, *39*, 15373–15379. [[CrossRef](#)]
6. Chen, X.; Wu, Z.; Gao, Z.; Ye, B.C. Effect of Different Activated Carbon as Carrier on the Photocatalytic Activity of Ag-N-ZnO Photocatalyst for Methyl Orange Degradation under Visible Light Irradiation. *Nanomaterials* **2017**, *7*, 258. [[CrossRef](#)]
7. Zheng, X.; Dong, Y.; Liu, T. Simultaneous photodegradation of dyes by NiS/CuS-CdS composites in visible light region. *Colloids Surf. A Physicochem. Eng. Asp.* **2020**, *598*, 124854. [[CrossRef](#)]
8. Inoue, T.; Fujishima, A.; Konishi, S.; Honda, K. Photoelectrocatalytic reduction of carbon dioxide in aqueous suspensions of semiconductor powders. *Nature* **1979**, *277*, 637–638. [[CrossRef](#)]
9. Chinh, V.; Hung, L.; Palma, L.; Hanh, V.; Vilardi, G. Effect of Carbon Nanotubes and Carbon Nanotubes/Gold Nanoparticles Composite on the Photocatalytic Activity of TiO₂ and TiO₂-SiO₂. *Chem. Eng. Technol.* **2019**, *42*, 308–315. [[CrossRef](#)]
10. Chinh, V.D.; Broggi, A.; Di Palma, L.; Scarsella, M.; Speranza, G.; Vilardi, G.; Thang, P.N. XPS Spectra Analysis of Ti²⁺, Ti³⁺ Ions and Dye Photodegradation Evaluation of Titania-Silica Mixed Oxide Nanoparticles. *J. Electron. Mater.* **2018**, *47*, 2215–2224. [[CrossRef](#)]
11. Yasmeeen, H.; Zada, A.; Ali, S.; Khan, I.; Ali, W.; Khan, W.; Khan, M.; Anwar, N.; Ali, A.; Huerta-Flores, A.M.; et al. Visible light-excited surface plasmon resonance charge transfer significantly improves the photocatalytic activities of ZnO semiconductor for pollutants degradation. *J. Chin. Chem. Soc.* **2020**, *67*, 1611–1617. [[CrossRef](#)]
12. Liu, W.; Wang, M.; Xu, C.; Chen, S.; Fu, X. Ag₃PO₄/ZnO: An efficient visible-light-sensitized composite with its application in photocatalytic degradation of Rhodamine B. *Mater. Res. Bull.* **2013**, *48*, 106–113. [[CrossRef](#)]
13. Ghasemi, S.; Hashemian, S.; Alamolhoda, A.; Gocheva, I.; Rahman, S. Plasmon enhanced photocatalytic activity of Au@TiO₂-graphene nanocomposite under visible light for degradation of pollutants. *Mater. Res. Bull.* **2017**, *87*, 40–47. [[CrossRef](#)]
14. Suyana, P.; Ganguly, P.; Nair, B.; Mohamed, A.; Warriar, K.; Hareesh, U. Co₃O₄-C₃N₄ p-n nano-heterojunctions for the simultaneous degradation of a mixture of pollutants under solar irradiation. *Environ. Sci. Nano* **2017**, *4*, 212–221. [[CrossRef](#)]
15. He, K.; Guo, L. NiS modified CdS pyramids with stacking fault structures: Highly efficient and stable photocatalysts for hydrogen production from water. *Int. J. Hydrogen Energy* **2017**, *42*, 23995–24005. [[CrossRef](#)]
16. Zhang, L.; Fu, X.; Meng, S.; Jiang, X.; Wang, J.; Chen, S. Ultra-low content of Pt modified CdS nanorods: One-pot synthesis and high photocatalytic activity for H₂ production under visible light. *J. Mater. Chem. A* **2015**, *3*, 23732–23742. [[CrossRef](#)]
17. Wang, J.; Li, H.; Meng, S.; Zhang, L.; Fu, X.; Chen, S. One-pot hydrothermal synthesis of highly efficient SnOx/Zn₂SnO₄ composite photocatalyst for the degradation of methyl orange and gaseous benzene. *Appl. Catal. B* **2017**, *200*, 19–30. [[CrossRef](#)]
18. Xiong, S.; Zhang, X.; Qian, Y. CdS with Various Novel Hierarchical Nanostructures by Nanobelts/Nanowires Self-Assembly: Controllable Preparation and Their Optical Properties. *Cryst. Growth Des.* **2009**, *9*, 5259–5265. [[CrossRef](#)]
19. Zhao, M.; Li, H.; Shen, X.; Ji, Z.; Xu, K. Facile electrochemical synthesis of CeO₂@Ag@CdS nanotube arrays with enhanced photoelectrochemical water splitting performance. *Dalton Trans.* **2015**, *44*, 19935–19941. [[CrossRef](#)]

20. Lu, X.-H.; Xie, S.-L.; Zhai, T.; Zhao, Y.-F.; Zhang, P.; Zhang, Y.-L.; Tong, Y.-X. Monodisperse CeO₂/CdS heterostructured spheres: One-pot synthesis and enhanced photocatalytic hydrogen activity. *RSC Adv.* **2011**, *1*, 1207–1210. [[CrossRef](#)]
21. Sultana, S.; Mansingh, S.; Scurrill, M.; Parida, K. Controlled Synthesis of CeO₂NS-Au-CdSQDs Ternary Nanoheterostructure: A Promising Visible Light Responsive Photocatalyst for H₂ Evolution. *Inorg. Chem.* **2017**, *56*, 12297–12307. [[CrossRef](#)] [[PubMed](#)]
22. Jin, J.; Fu, M.; Wang, L.; Ma, T.; Li, X.; Jin, F.; Lu, Y. Water-splitting mechanism analysis of Sr/Ca doped LaFeO₃ towards commercial efficiency of solar thermochemical H₂ production. *Int. J. Hydrogen Energy* **2021**, *46*, 1634–1641. [[CrossRef](#)]
23. Liu, S.; Wu, X.; Liu, W.; Chen, W.; Ran, R.; Li, M.; Weng, D. Soot oxidation over CeO₂ and Ag/CeO₂: Factors determining the catalyst activity and stability during reaction. *J. Catal.* **2016**, *337*, 188–198. [[CrossRef](#)]
24. Liu, X.; Zhou, K.; Wang, L.; Wang, B.; Li, Y. Oxygen vacancy clusters promoting reducibility and activity of ceria nanorods. *J. Am. Chem. Soc.* **2009**, *131*, 3140–3141. [[CrossRef](#)]
25. Mai, H.; Sun, L.; Zhang, Y.; Si, R.; Feng, W.; Zhang, H.; Liu, H.; Yan, C. Shape-selective synthesis and oxygen storage behavior of ceria nanopolyhedra, nanorods, and nanocubes. *J. Phys. Chem. B* **2005**, *109*, 24380–24385. [[CrossRef](#)] [[PubMed](#)]
26. Khan, M.; Ansari, S.; Ansari, M.O.; Min, B.; Lee, J.; Cho, M. Biogenic Fabrication of Au@CeO₂ Nanocomposite with Enhanced Visible Light Activity. *J. Phys. Chem. C* **2014**, *118*, 9477–9484. [[CrossRef](#)]
27. Primo, A.; Marino, T.; Corma, A.; Molinari, R.; Garcia, H. Efficient visible-light photocatalytic water splitting by minute amounts of gold supported on nanoparticulate CeO₂ obtained by a biopolymer templating method. *J. Am. Chem. Soc.* **2011**, *133*, 6930–6933. [[CrossRef](#)] [[PubMed](#)]
28. Kundu, S.; Ciston, J.; Senanayake, S.; Arena, D.; Fujita, E.; Stacchiola, D.; Barrio, L.; Navarro, R.; Fierro, J.; Rodriguez, J. Exploring the Structural and Electronic Properties of Pt/Ceria-Modified TiO₂ and Its Photocatalytic Activity for Water Splitting under Visible Light. *J. Phys. Chem. C* **2012**, *116*, 14062–14070. [[CrossRef](#)]
29. Zhou, Y.; Yang, J.; He, T.; Shi, H.; Cheng, X.; Lu, Y. Highly stable and dispersive silver nanoparticle-graphene composites by a simple and low-energy-consuming approach and their antimicrobial activity. *Small* **2013**, *9*, 3445–3454. [[CrossRef](#)]
30. Feng, C.; Chen, Z.; Li, W.; Zhou, J.; Sui, Y.; Xu, L.; Sun, M. Effectively enhanced photocatalytic degradation performance of the Ag-modified porous ZnO nanorod photocatalyst. *J. Mater. Sci. Mater. Electron.* **2018**, *29*, 9301–9311. [[CrossRef](#)]
31. Tao, X.; Zhou, Y.; Xu, K.; Wu, Y.; Mi, J.; Li, Y.; Liu, Q.; Cheng, X.; Zhao, N.; Shi, H.; et al. Bifunctional Material with Organic Pollutant Removing and Antimicrobial Properties: Graphene Aerogel Decorated with Highly Dispersed Ag and CeO₂ nanoparticles. *ACS Sustain. Chem. Eng.* **2018**, *6*, 16907–16919. [[CrossRef](#)]
32. Jiao, J.; Wei, Y.; Zhao, Z.; Liu, J.; Li, J.; Duan, A.; Jiang, G. Photocatalysts of 3D Ordered Macroporous TiO₂-Supported CeO₂ Nanolayers: Design, Preparation, and Their Catalytic Performances for the Reduction of CO₂ with H₂O under Simulated Solar Irradiation. *Ind. Eng. Chem. Res.* **2014**, *53*, 17345–17354. [[CrossRef](#)]
33. Zheng, N.; Ouyang, T.; Chen, Y.; Wang, Z.; Chen, D.; Liu, Z. Ultrathin CdS shell-sensitized hollow S-doped CeO₂ spheres for efficient visible-light photocatalysis. *Catal. Sci. Technol.* **2019**, *9*, 1357–1364. [[CrossRef](#)]
34. Yu, L.; Peng, R.; Chen, L.; Fu, M.; Wu, J.; Ye, D. Ag supported on CeO₂ with different morphologies for the catalytic oxidation of HCHO. *Chem. Eng. J.* **2018**, *334*, 2480–2487. [[CrossRef](#)]
35. Chang, S.; Li, M.; Hua, Q.; Zhang, L.; Ma, Y.; Ye, B.; Huang, W. Shape-dependent interplay between oxygen vacancies and Ag–CeO₂ interaction in Ag/CeO₂ catalysts and their influence on the catalytic activity. *J. Catal.* **2012**, *293*, 195–204. [[CrossRef](#)]
36. Wang, Y.; Li, B.; Zhang, C.; Cui, L.; Kang, S.; Li, X.; Zhou, L. Ordered mesoporous CeO₂-TiO₂ composites: Highly efficient photocatalysts for the reduction of CO₂ with H₂O under simulated solar irradiation. *Appl. Catal. B Environ.* **2013**, *130–131*, 277–284. [[CrossRef](#)]
37. Ma, Y.; Bian, Y.; Liu, Y.; Zhu, A.; Wu, H.; Cui, H.; Chu, D.; Pan, J. Construction of Z-Scheme System for Enhanced Photocatalytic H₂ Evolution Based on CdS Quantum Dots/CeO₂ Nanorods Heterojunction. *ACS Sustain. Chem. Eng.* **2018**, *6*, 2552–2562. [[CrossRef](#)]
38. Tao, Y.; Wang, H.; Xia, Y.; Zhang, G.; Wu, H.; Tao, G. Preparation of shape-controlled CeO₂ nanocrystals via microwave-assisted method. *Mater. Chem. Phys.* **2010**, *124*, 541–546. [[CrossRef](#)]
39. Duan, H.; Xuan, Y. Synthesis and optical absorption of Ag/CdS core/shell plasmonic nanostructure. *Sol. Energy Mater. Sol. Cells* **2014**, *121*, 8–13. [[CrossRef](#)]
40. Guan, S.; Fu, X.; Tang, Y.; Peng, Z. Synthesis and photoelectrochemical performance of AuAg@CdS double-walled nanotubes. *Chem. Phys. Lett.* **2017**, *682*, 128–132. [[CrossRef](#)]
41. Kuriakose, A.; Nampoori, V.; Thomas, S. Influence of laser ablated Ag core on the thermo-optic and photocatalytic characteristics of CdS nanocolloids. *Mater. Chem. Phys.* **2021**, *258*, 123911. [[CrossRef](#)]
42. Guo, Y.; Mei, S.; Yuan, K.; Wang, D.; Liu, H.; Yan, C.; Zhang, Y. Low-Temperature CO₂ Methanation over CeO₂-Supported Ru Single Atoms, Nanoclusters, and Nanoparticles Competitively Tuned by Strong Metal-Support Interactions and H-Spillover Effect. *ACS Catal.* **2018**, *8*, 6203–6215. [[CrossRef](#)]
43. Sastre, F.; Puga, A.; Liu, L.; Corma, A.; Garcia, H. Complete photocatalytic reduction of CO₂ to methane by H₂ under solar light irradiation. *J. Am. Chem. Soc.* **2014**, *136*, 6798–6801. [[CrossRef](#)]
44. Peng, R.; Sun, X.; Li, S.; Chen, L.; Fu, M.; Wu, J.; Ye, D. Shape effect of Pt/CeO₂ catalysts on the catalytic oxidation of toluene. *Chem. Eng. J.* **2016**, *306*, 1234–1246. [[CrossRef](#)]
45. Singhanian, N.; Anumol, E.; Ravishankar, N.; Madras, G. Influence of CeO₂ morphology on the catalytic activity of CeO₂-Pt hybrids for CO oxidation. *Dalton Trans.* **2013**, *42*, 15343–15354. [[CrossRef](#)]

46. Shen, H.; Xue, T.; Wang, Y.; Cao, G.; Lu, Y.; Fang, G. Photocatalytic property of perovskite LaFeO_3 synthesized by sol-gel process and vacuum microwave calcination. *Mater. Res. Bull.* **2016**, *84*, 15–24. [[CrossRef](#)]
47. Tian, S.; Tu, Y.; Chen, D.; Chen, X.; Xiong, Y. Degradation of Acid Orange II at neutral pH using $\text{Fe}_2(\text{MoO}_4)_3$ as a heterogeneous Fenton-like catalyst. *Chem. Eng. J.* **2011**, *169*, 31–37. [[CrossRef](#)]
48. Chinh, V.; Bavasso, I.; Palma, L.; Felici, A.; Scarsella, M.; Vilardi, G.; Bracciale, M.; Van, N. Enhancing the photocatalytic activity of TiO_2 and $\text{TiO}_2\text{-SiO}_2$ by coupling with graphene-gold nanocomposites. *J. Mater. Sci. Mater. Electron.* **2021**, *32*, 5082–5093. [[CrossRef](#)]
49. Zhang, L.; Long, J.; Pan, W.; Zhou, S.; Zhu, J.; Zhao, Y.; Wang, X.; Cao, G. Efficient removal of methylene blue over composite-phase BiVO_4 fabricated by hydrothermal control synthesis. *Mater. Chem. Phys.* **2012**, *136*, 897–902. [[CrossRef](#)]
50. Berglund, S.; Flaherty, D.; Hahn, N.; Bard, A.; Mullins, C. Photoelectrochemical Oxidation of Water Using Nanostructured BiVO_4 Films. *J. Phys. Chem. C* **2011**, *115*, 3794–3802. [[CrossRef](#)]
51. Bi, J.; Zhou, Z.; Chen, M.; Liang, S.; He, Y.; Zhang, Z.; Wu, L. Plasmonic Au/CdMoO_4 photocatalyst: Influence of surface plasmon resonance for selective photocatalytic oxidation of benzylic alcohol. *Appl. Surf. Sci.* **2015**, *349*, 292–298. [[CrossRef](#)]
52. Hou, Y.; Zuo, F.; Dagg, A.; Feng, P. Visible light-driven $\alpha\text{-Fe}_2\text{O}_3$ nanorod/graphene/ $\text{BiV}_{1-x}\text{Mo}_x\text{O}_4$ core/shell heterojunction array for efficient photoelectrochemical water splitting. *Nano Lett.* **2012**, *12*, 6464–6473. [[CrossRef](#)] [[PubMed](#)]